

An *XMM-Newton* and *Chandra* Study of the Starburst Galaxy IC 10Q. Daniel Wang, Katherine E. Whitaker, & Rosa Williams¹*Astronomy Department, University of Massachusetts, Amherst, MA 01003, USA***ABSTRACT**

We present an X-ray study of our nearest starburst galaxy IC 10, based on *XMM-Newton* and *Chandra* observations. A list of 73 *XMM-Newton* and 28 *Chandra* detections of point-like X-ray sources in the field is provided; a substantial fraction of them are likely stellar objects in the Milky Way due to the low Galactic latitude location of IC 10. The brightest source in the IC 10 field, X-1, has a mean 0.3-8.0 keV luminosity of $\sim 1.2 \times 10^{38}$ erg s⁻¹ and shows a large variation by a factor of up to ~ 6 on time scales of $\sim 10^4$ s during the *XMM-Newton* observation. The X-ray spectra of the source indicate the presence of a multi-color blackbody accretion disk with an inner disk temperature $T_{in} \approx 1.1$ keV. These results are consistent with the interpretation of the source as a stellar mass black hole, probably accreting from a Wolf-Rayet star companion. We infer the mass of this black hole to be $\sim 4 M_{\odot}$ if it is not spinning, or a factor of up to ~ 6 higher if there is significant spinning. We also detect an apparent diffuse soft X-ray emission component of IC 10. An effective method is devised to remove the X-ray CCD-readout streaks of X-1 that strongly affect the study of the diffuse component in the *XMM-Newton* and *Chandra* observations. We find that the diffuse X-ray morphology is oriented along the optical body of the galaxy and is chiefly associated with starburst regions. The diffuse component can be characterized by an optically thin thermal plasma with a mean temperature of $\sim 4 \times 10^6$ K and a 0.5-2 keV luminosity of $\sim 8 \times 10^{37}$ erg s⁻¹, representing only a small fraction of the expected mechanical energy inputs from massive stars in the galaxy. There is evidence that the hot gas is driving outflows from the starburst regions; therefore, the bulk of the energy inputs may be released in a galactic wind.

¹Currently at Astronomy Department, University of Illinois at Urbana-Champaign, 1002 West Green Street, Urbana, IL 61801

1. Introduction

X-ray observations are the most sensitive tool available for the study of massive star end products, both stellar and interstellar. IC 10 is our nearest laboratory for such a study in a dwarf starburst galaxy. This galaxy is particularly known for its large number of Wolf-Rayet (W-R) stars; the global surface density, ~ 40 W-R kpc^{-2} over an area of ~ 2.5 kpc^{-2} , is about 20 times higher than in the Large Magellanic Cloud (Richer et al. 2001; Massey & Holmes 2002). This large population of W-R stars is very unusual for the low metallicity of IC 10 ($\sim 15\%$ solar; e.g., Lequeux et al. 1979; Crowther et al. 2003). The galaxy also contains a number of energetic interstellar shells; their origins are, however, unclear (e.g., Wilcots & Miller 1998; Yang & Skillman 1993). The presence of an enigmatic radio emission shell of diameter ~ 140 pc around the brightest X-ray source IC 10 X-1 is particularly interesting (Yang & Skillman 1993; Bauer & Brandt 2004). The radio emission is predominantly nonthermal, as indicated by its steep spectrum. The required presence of an extremely powerful source of relativistic particles is *not* expected for a typical shell-like supernova remnant on such a large scale or for a young superbubble produced by an OB association, which would generate overwhelming amounts of ionizing radiation. Indeed, the shell shows only weak $\text{H}\alpha$ (or thermal) emission (Yang & Skillman 1993). It has been suggested that the nonthermal radio shell may be powered by IC 10 X-1, similar to the link between the Galactic X-ray binary SS 433 and its surrounding nonthermal structure W50 (diameter $\sim 50 \times 100$ pc), albeit on greater physical and energetic scales (Brandt et al. 1997; Bauer & Brandt 2004).

IC 10 X-1 is the focus of the previous X-ray studies by Brandt et al. (1997) and Bauer & Brandt (2004). They find that the source is spatially coincident with the W-R star [MAC92] 17A in IC 10 (Massey, Armanroff, & Conti 1992) and speculate that the accreting compact object is a black hole (BH) based on its high X-ray luminosity, strong variability, and the high mass of this likely companion star. It is of great interest to confirm the identity of this compact object, which is comparable in many ways to Cyg X-3 — a candidate for a rare class of compact star/W-R binaries, which may shed light onto the differing pre-supernova evolutionary scenarios for very massive stars (Clark & Crowther 2004).

Here we present our *XMM-Newton* observations of IC 10, together with a re-analysis of the *Chandra* data studied by Bauer & Brandt (2004). These two complementary data sets together give us a comprehensive X-ray view of the galaxy. The *Chandra* data provide us with arcsecond spatial resolution, important for isolating point-like sources, especially in regions close to X-1. But the data, taken with the detector ACIS-S in a (500 pixel) sub-array mode, covers only a portion of the galaxy. In addition, the significant pile-up of X-1 adds a degree of spectral complexity (Davis 2001; Bauer & Brandt 2004). Furthermore, the

CCD-readout streak of the source significantly contaminates the “diffuse” X-ray component observed. The *XMM-Newton* observations provide both a higher effective photon-collecting area and a larger field coverage than the *Chandra* observation, albeit with a substantially poorer resolution (FWHM $\sim 13''$). While the pile-up of X-1 is not an issue for the *XMM-Newton* observations, the CCD-readout streak contamination is serious. Therefore, we need to remove these streaks in order to correctly map out the diffuse X-ray component of IC 10.

In this work, we adopt the distance of IC 10 to be ~ 0.7 Mpc (hence $1' = 204$ pc; Demers, Battinelli, & Letarte 2004 and references therein). While data points in plots are shown all with 1σ error bars, our quoted parameter uncertainty ranges are at the 90% confidence level unless otherwise noted.

2. Observations and Data Calibration

2.1. *XMM-Newton* Data

The *XMM-Newton* observations were taken on July 3, 2003 with a total exposure time of ~ 45 ks for the EPIC-MOS cameras and ~ 42 ks for the EPIC-PN camera. We use only the data from the PN camera (with a thin optical blocking filter) because of its high sensitivity to soft X-rays in the study of diffuse emission and include the data from the MOS cameras in the analysis of X-1. The data from the RGS and OM provide no useful information here and are thus not presented here.

We calibrate the data with the SAS software (version 6.1.0), together with the latest calibration files. For the MOS data, we include only events with patterns 0 through 12, and the standard MOS flags (XMMEA_EM). The PN events are filtered to include only events with patterns 0 through 4, and the PN flags (XMMEA_EP, XMMEA_2, and XMMEA_3). We exclude time intervals with strong flares to reduce the non-cosmic X-ray background, which is due to cosmic-ray induced events, instrumental fluorescence, and soft protons that are funneled towards the detectors by the X-ray mirrors. We find that the flaring is consistent in the 0.3-2 keV and 10-15 keV bands, in which the light curves of the observations are examined. We thus remove time intervals with significant count rate (CR) deviations from the mean in the 0.3-2 keV band. The chosen threshold is 0.8 counts s^{-1} for the MOS and 2.0 counts s^{-1} for the PN data. This filtering leaves a total accepted net exposure time of ~ 35.5 ks for each of the two MOS cameras and ~ 32 ks for the PN camera.

For the PN data, we construct maps in the 0.5-1, 1-2, 2-4.5, and 4.5-7.5 keV bands. We have also examined the data in the 0.2-0.5 keV band, but find that it contains too many artifacts and little X-ray emission from IC 10. We generate corresponding effective

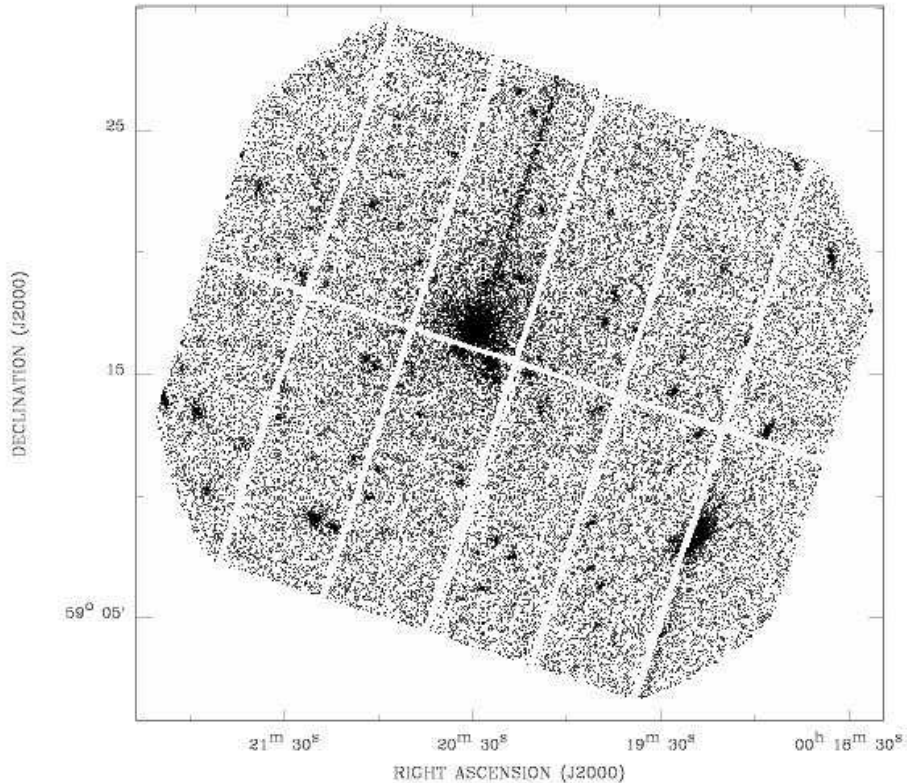


Fig. 1.— *XMM-Newton* EPIC-PN image in the 0.5-7.5 keV band. The image’s northwest and southeast edges (each 1′.5 wide) have been removed for high instrument background and are not used in our data analysis. The CCD-readout streak of the brightest source X-1 is apparent in chip # 4. The bright source in the lower right chip also produces a faint but visible streak, which does not significantly affect our analysis and is thus not removed here.

exposure images, using the SAS program *eeexpmap*. These exposure maps correct for various instrumental artifacts, including bad pixels and columns, the detector quantum efficiency non-uniformity, filter transmission, and telescope vignetting. Such a correction is made on a count image after the removal of a background, which is partly due to non-cosmic X-rays not vignettted by the telescope. We generate the background data, using the *skycast* program and the “blank sky” database — source-removed high Galactic latitude observations with a total exposure of 352 ks (Read & Ponman 2003). The background data are processed with the same filters as used for the IC 10 observations.

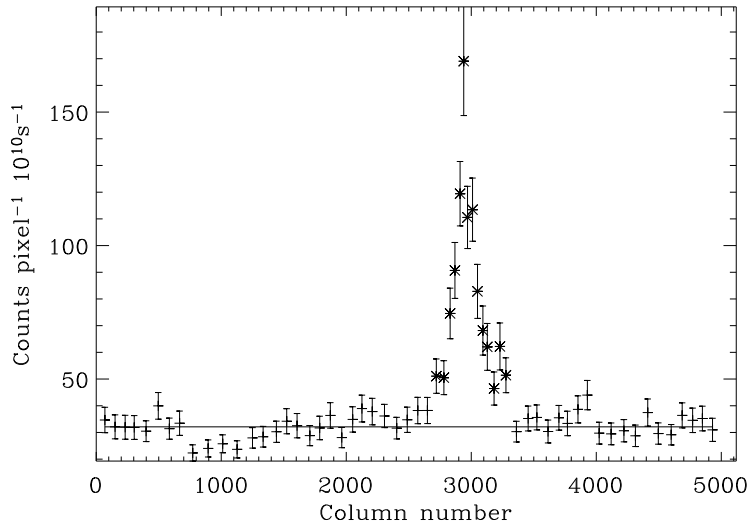


Fig. 2.— *XMM-Newton* EPIC-PN intensity profile across the CCD chip # 4 along the direction perpendicular to the CCD readout columns (Fig. 1). The regions around X-1 and other sources are removed in the intensity calculation. The columns marked with “×” are considered to be significantly affected by the streak. The intensity excess of the columns above the average (the horizontal line) over the unaffected ranges is considered to be the streak contribution.

2.2. CCD-readout Streak Removal

The most outstanding artifact in the *XMM-Newton* data is the southeast-northwest streak (Fig. 1), which was caused by the continuous exposure of the PN CCD (# 4) to X-1 during its readout. This streak spreads the counts (statistically) evenly into columns along the read-out direction of the CCD. Such a streak is typically removed by replacing the affected columns with events randomly generated from an estimated background spectrum. This simple cosmetic repair, however, would also remove any sources and/or extended structures in the columns and would create new artifacts, especially in regions near X-1. We have developed a more effective streak removal method. We calculate the average intensity distribution as a function of the column number across the CCD chip (Fig. 2), after excluding regions that are significantly affected by diffuse or scattered X-1 emission as well as individual detected sources (to be discussed later). The calculated streak contribution is then cast into the sky coordinates. The resultant streak image can then be subtracted from the observed X-ray intensity image. Fig. 3 shows such a “streak-free”, background-removed, and flat-fielded intensity image in the 0.5-4.5 keV band. The streak produces no apparent

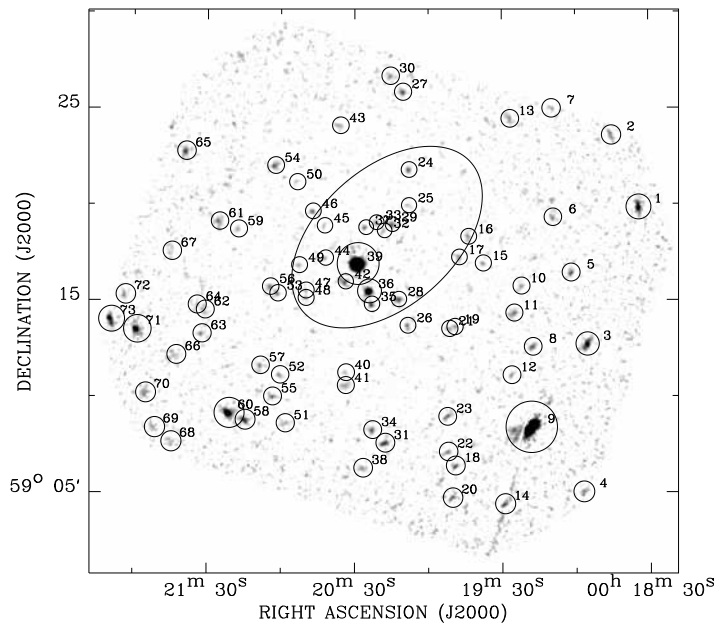


Fig. 3.— EPIC-PN intensity image in the 0.5-7.5 keV band after the CCD streak removal (Fig. 1) and flat-fielding. The circles outline the source regions (two times the 50% EER), which are to be removed for diffuse X-ray analysis. An adaptively smoothed background has also been subtracted from the image to highlight discrete sources. The source numbers (Table 1) are marked. The ellipse outlines the 2MASS “total” size of IC 10 in the K_s band (Jarrett et al. 2003).

effect in lower or higher energy bands. A streak image in a sub-energy band can easily be produced with a normalization of the relative intensity of the streak.

2.3. *Chandra* Data

The *Chandra* observation, taken on March 12, 2003 with an exposure of 29 ks, has already been described by Bauer & Brandt (2004). We reprocess the data, using the latest CIAO software (version 3.2.1) and calibration database (version 3.0.0), following the same procedure as detailed in Wang et al. (2003). We create ACIS-S images and corresponding exposure (flat-fielding) images in the 0.3-0.7, 0.7-1.5, 1.5-3, and 3-7 keV bands.

A CCD-readout streak similar to that seen in the PN data is also found in the *Chandra* ACIS-S image in the 0.7-3 keV range (Fig. 4a). We remove this CCD-readout streak in the

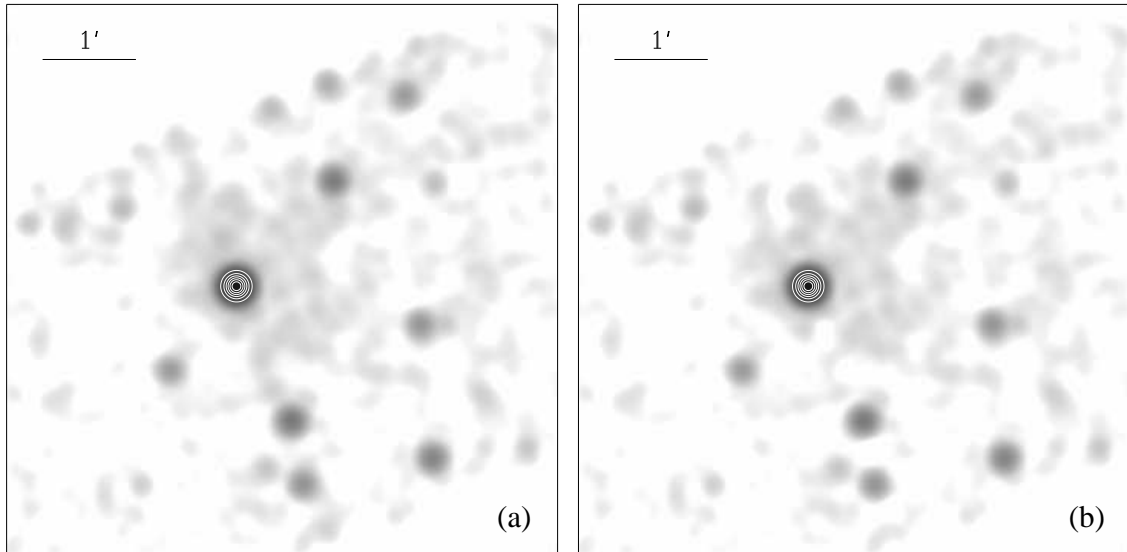


Fig. 4.— *Chandra* ACIS-S images in the 0.7-3 keV band (a) before and (b) after the CCD-readout streak removal. The images have been smoothed with a Gaussian of FWHM=12'' .

same way as used for the PN data. The total number of counts contributed by the streak is only about 92, a 5σ excess above the local background. The streak-removed image is shown in Fig. 4b.

The *Chandra* observation has a superb on-axis resolution of 90% EER= 1 – 2'' within $\sim 4'$. However, the PSF degrades steeply at larger off-axis angles. The *XMM-Newton* PSF is relatively uniform across much of the PN field of view. Therefore, our use of the *Chandra* data is limited within the central region as shown in Fig. 5.

3. Data Analysis and Results

3.1. Discrete Sources

We use an IDL-based program to detect sources in both the *Chandra* ACIS-S and the *XMM-Newton* PN data. As in the previous applications (e.g., Wang et al. 2003; Wang 2004a), this program, optimized to detect point-like sources, uses a combination of detection algorithms: wavelet, sliding-box, and maximum likelihood centroid fitting. First, we construct the ‘Mexican cap’ wavelet images on scales of 1, 2, 4 and 8 image bins (bin size = 4'' for the PN and 0.5'' for the ACIS-S). On each scale we search for source candidates correspond-

ing to local maxima with signal-to-noise ratios $S/N > 2.5$. Next, we apply a map detection (‘sliding box’ method) with a background map produced by excising the source candidates and adaptively smoothing the map to achieve a local count-to-noise ratio greater than 10. Finally, the sources detected with the map method are analyzed by a maximum likelihood algorithm, using both the background map and an approximate Gaussian PSF. This analysis gives optimal source positions and their 1σ errors. The source detection in both the map detection and the maximum likelihood analysis is based on data within the 50% PSF energy-encircled radius (EER) for the PN data and the 90% EER for the ACIS-S data. The final accepted sources all have the individual false detection probability $P \leq 10^{-6}$ (ACIS-S) and 10^{-7} (PN). The processed PN data still contain various residual artifacts (more significant than in the ACIS-S data); the chosen stringent detection threshold minimizes their effect in the source detection.

The source detections are carried out in the broad (B), soft (S), and hard (H) bands, defined differently for the ACIS-S and PN data sets in the notes to Tables 1 and 2. For each data set, the detected sources in the three bands are merged together. Multiple detections with overlapping 2σ centroid error circles are considered to be the same source, and the centroid with the smallest error is adopted.

Tables 1 and 2 summarize the results from our source detection in the two data sets. For ease of reference, we will refer to X-ray sources detected in the *XMM-Newton* PN and *Chandra* ACIS data sets with the prefixes XP and XA, respectively (e.g., XP-13). The source locations are marked in the X-ray intensity images (Figs. 3 and 5). The detection reveals many more sources in the *Chandra* data than in the *XMM-Newton* data in the overlapping region around X-1. Part of this difference is due to the limited spatial resolution of the *XMM-Newton* instrument; the source detection sensitivity is very much affected by the PSF of X-1 and the presence of the diffuse emission, as well as source confusion. Nevertheless, most bright X-ray sources in the *Chandra* field are also detected with the *XMM-Newton* data. Several relatively bright sources, such as XA-13, XA-17, and XP-49 (the PN source next to XA-35 in Fig. 5), should have been detected in both data sets. The fact that they appear only in one data set indicates their strong variability from one observation to another.

We may further use the *XMM-Newton* and *Chandra* data sets to provide limited X-ray spectral information on the detected sources. Most of the *XMM-Newton* detected sources are apparently outside the optical/near-IR main body of IC 10 and are probably unrelated to the galaxy (Fig. 3). The *Chandra* detected sources, on the other hand, are more likely to be associated with the galaxy. We thus extract an accumulated ACIS-S spectrum of the sources located in the S3 chip, excluding sources that are located at the edges (i.e., XA-12, 16, and 23; Fig. 5). This spectrum can be characterized ($\chi^2/dof = 11/29$) by a power law with a photon

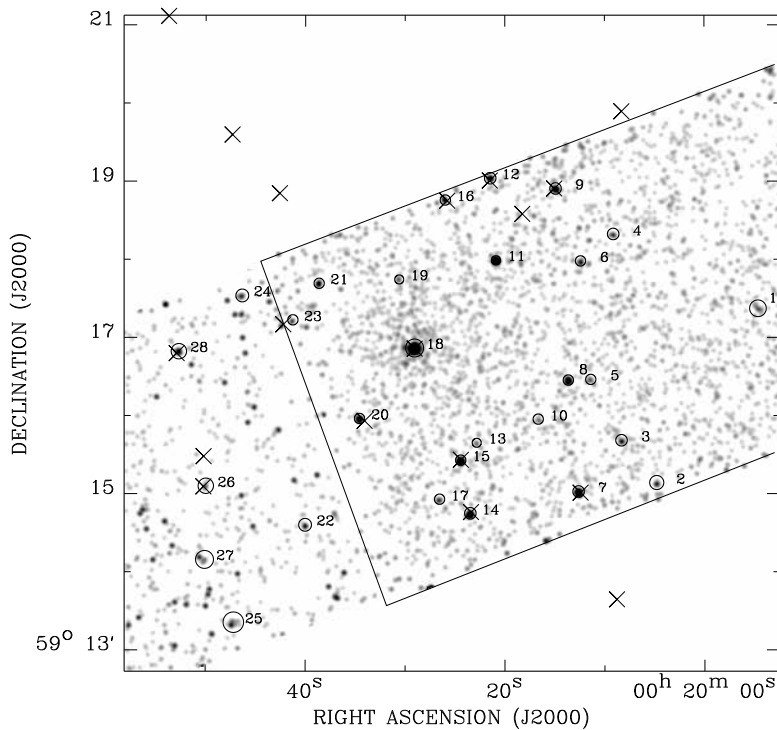


Fig. 5.— *Chandra* ACIS-S intensity image in the 0.3-7 keV band after the CCD streak is removed and flat-fielded. The field covered by the on-axis S7 chip is outlined; the remaining (low left) coverage of the image is from part of the S2 chip. The circles represent the source regions (two times the 90% EER), which are to be removed for diffuse X-ray analysis. The source numbers (Table 2) are also marked. Positions of *XMM-Newton* PN sources in the field are represented by crosses.

index of 1.2(0.89 - 1.6) and an absorption column density $N_H = 1.8(0.9 - 2.9) \times 10^{21} \text{ cm}^{-2}$ (Fig. 6). Although the constraints on the spectral parameters are generally weak, the index is consistent with the value ($\sim 1 - 2$) expected for typical high-mass X-ray binaries. The N_H is considerably lower than that expected total absorption toward sources inside IC 10; the Galactic H I absorption alone is $N_{HI} = 4.8 \times 10^{21} \text{ cm}^{-2}$ (Stark et al. 1992). The absorption-corrected luminosity of the sources is $3 \times 10^{37} \text{ erg s}^{-1}$ in the 0.3-8 keV band. Therefore, the spectrum, especially in the low energy part, may still significantly be contaminated by Galactic objects.

For relatively bright sources, we give hardness ratios to constrain individual spectral properties (Tables 1 and 2). Most of the calculated ratios are consistent with a power law that has an index in the range of 1-3, together with a foreground absorption $N_H =$

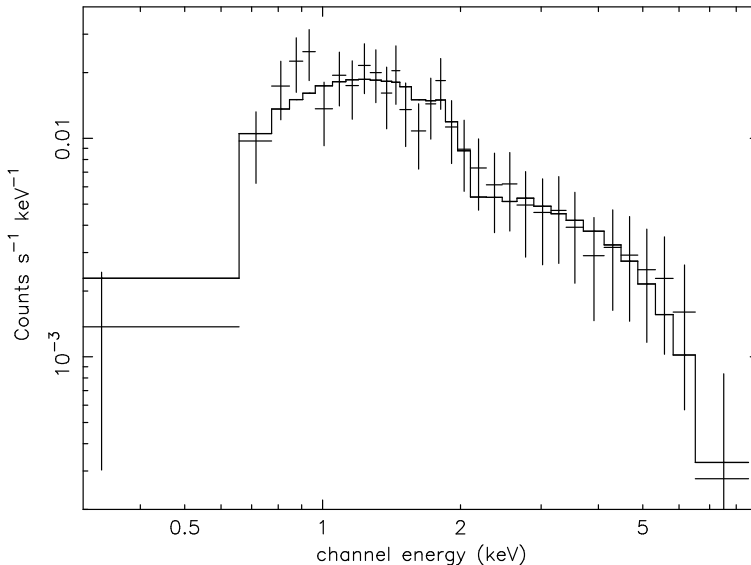


Fig. 6.— Accumulated ACIS-S spectrum of *Chandra*-detected sources on the S3 chip (Fig. 5), together with the best-fit power law model. The spectrum is binned with a minimum number of counts to be 25.

$(0.3 - 3) \times 10^{22} \text{ cm}^{-2}$. Such sources are probably X-ray binaries in IC 10 or background AGNs. Soft X-ray sources, especially those with HR1 values $\lesssim 0.3$ (Table 1), should be in our Galaxy (§4.1), because the inferred N_H is less than the accepted Galactic absorption. Most of the other sources are too faint to be constrained individually. A useful, though crude, conversion factor from a count rate (in either Table 1 or 2) to an absorption-corrected energy flux in the 0.5-8 keV band is $\sim 2.3 \times 10^{-11} \text{ (erg cm}^{-2} \text{ s}^{-1})/(\text{counts s}^{-1})$ for a source with a power law of a photon index ~ 2 and a total X-ray-absorbing gas column density of $\sim 1 \times 10^{22} \text{ cm}^{-2}$, reasonable approximations for sources in IC 10 (see §4.1).

3.2. IC 10 X-1

The *XMM-Newton* observations show a large intensity variation of X-1, a factor of up to ~ 6 and 4 in the PN 0.5-2.0 keV and 2.0-7.5 keV bands and on a time scale of 10^4 s (Fig. 7). This amplitude is a factor of ~ 2 greater than that during the *Chandra* observation (Bauer & Brandt 2004). Similar variability is also seen in the MOS data. The large luminosity dip, as seen in the light curves, could be due to an eclipsing of the accreting compact source by its companion. We detect no apparent periodic signal; both the FFT power spectrum and the period folding analysis show too much confusion from the harmonics and their aliases of the CCD readout period (73.4 ms).

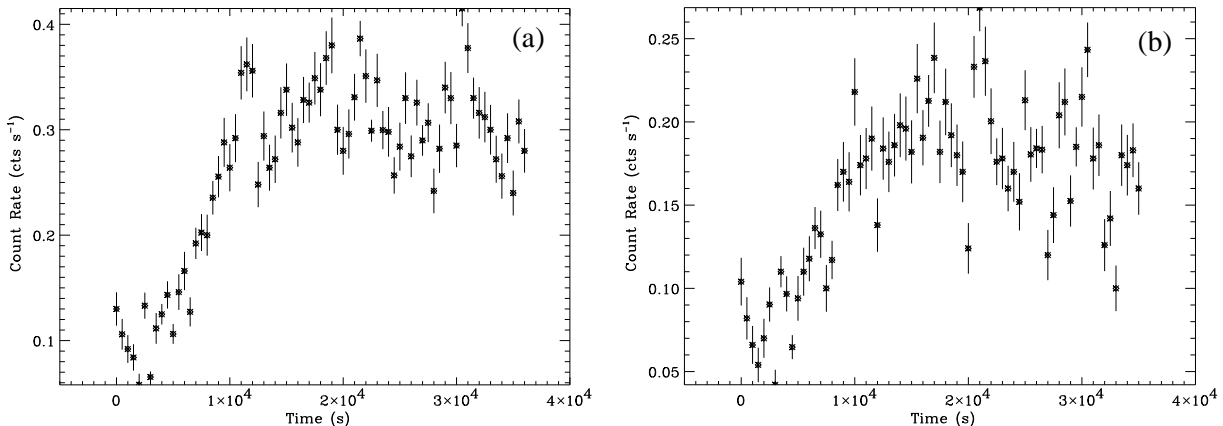


Fig. 7.— Variability of X-1 in the PN 0.5-2.0 keV (a) and 2.0-7.5 keV (b) bands. The events are shown in 500 s bins, with corrections for partially binning on Good Time Interval boundaries, accepting only bins with exposure greater than 25% of the bin width.

Fig. 8a shows that the *XMM-Newton* spectra of X-1 are nearly featureless (except for various instrumental features). We fit the spectra with various models that are typically used for X-ray binaries, together with a foreground photoelectric absorption. The overall metal abundance of the absorbing gas is allowed to vary, relative to hydrogen, although the relative metal abundances are fixed to the pattern of Balucinska-Church & McCammon (1992). We find that a simple power law model with a best-fit $\chi^2/dof = 1126/812$ can be ruled out with a null hypothesis probability of 10^{-12} ; the spectra appear to have an intrinsically blackbody-like convex shape. But the spectra are reasonably well characterized ($\chi^2/dof = 863/812$) by the multi-color disk model (MCD; i.e., *diskbb* in the *XSPEC* spectral analysis software package; Arnaud 1996; Makishima et al. 1986). The fitted inner disk temperature and radius are $T_{in} = 1.18(1.16 - 1.20)$ keV and $R_{in} = 15(14 - 16)/(\cos\theta)^{1/2}$ km, where θ is the inclination angle of the disk, while the absorption column density is $N_H = 1.25(1.20 - 1.29) \times 10^{22}$ cm $^{-2}$ with a metal abundance < 0.01 solar; a fit with the fixed solar metal abundances is not acceptable ($\chi^2/dof = 1045/813$). This unusually low metal abundance is probably not physical and may be due to uncertainties in the spectral calibration at low energies. The absorption-corrected luminosity of the source is 1.2×10^{38} erg s $^{-1}$ in the 0.3-8.0 keV band. Both the spectral shape and the luminosity of X-1 are very similar to those of the well-studied persistent X-ray binaries with stellar mass BHs (i.e., LMC X-1, LMC X-3, and Cyg X-1).

To further characterize the putative BH as well as the accretion disk of X-1, we fit the *XMM-Newton* spectra with a self-consistent Comptonized MCD (CMCD) model (Wang et al. 2004; Yao et al. 2005). This model is implemented in *XSPEC* as a table of spectra

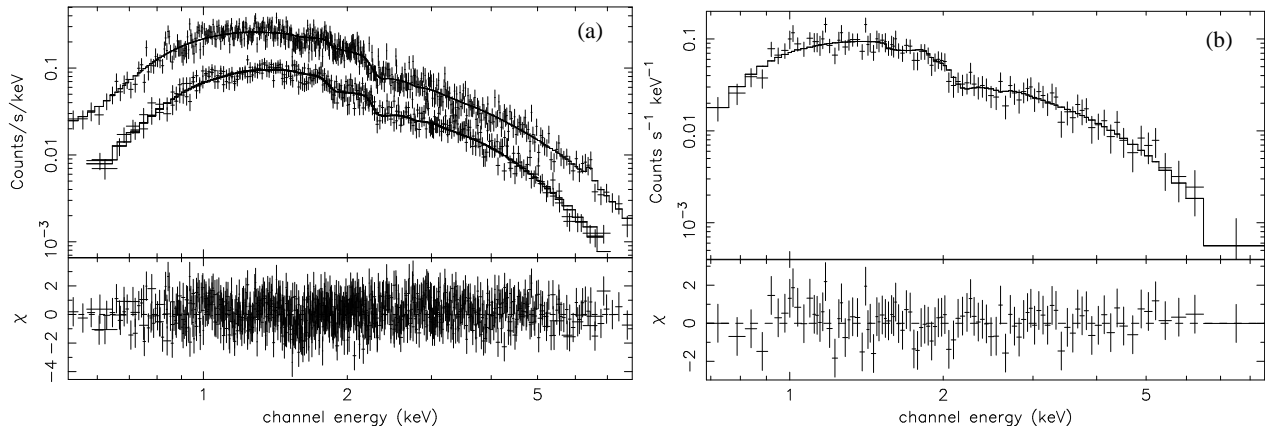


Fig. 8.— The PN+MOS (a) and ACIS-S (b) spectra of IC 10 X-1. The histograms show the best-fit CMCD model.

generated from Monte-Carlo simulations of the Comptonization, which assumes a spherically symmetric, thermal corona around an accretion disk. The fitted parameters of the CMCD model are the corona optical depth $\tau = 1.7(1.1 - 2.4)$, effective radius $R_c = 50(43 - 73)$ km, electron temperature $\lesssim 15$ keV, and disk inclination angle $\theta \lesssim 57^\circ$, as well as $T_{in} = 1.11(1.06 - 1.17)$ keV and $R_{in} = 25(19 - 29)$ km. The obtained N_H is almost the same as that obtained for the MCD model. The fit is satisfactory ($\chi^2/dof = 837/809$). Following Wang et al. (2004), we further infer the mass of the BH by assuming that R_{in} represents the radius of the last stable circular orbit, after correcting for various general relativity spectral hardening and Doppler shift effects (a factor of ~ 2 total correction). For a non-spinning BH, our inferred mass is $4.1(3.1, 4.9) M_\odot$, which depends weakly on θ (within its 90% uncertainty range). But for an extreme spinning BH, the mass could be a factor of up to 6 greater, sensitively depending on θ (see Fig. 2 in Wang et al. 2004).

There is a marginal presence of an emission line at ~ 6.4 keV, presumably representing the $K\alpha$ transition of neutral or weakly ionized iron. The inclusion of a narrow Gaussian line with the centroid fixed at this energy leads to a small improvement of the fit ($\chi^2/dof = 829/808$) and does not significantly change the parameters of the other spectral components. The luminosity of the line is $\sim 2.8(0 - 5.8) \times 10^{35}$ ergs s^{-1} , corresponding to an equivalent width of ~ 70 eV.

To test the spectral variability, we further extract two separate sets of spectra in the time intervals less and greater than 8000 s in Fig. 7. However, the total of PN+MOS counts in the lower flux interval is only about 470. The two spectra show no statistically significant difference.

For comparison with the *XMM-Newton* spectra, we further extract a *Chandra* ACIS-S spectrum of X-1 from a circle of $8''$ radius and a local background spectrum from a concentric annulus of radius $32''$ – $67''$. We use the newly improved CIAO routine *mkacisrmf* to generate the spectral response matrices and include Davis’s model for the pile-up correction (Davis 2001). Our obtained pile-up fraction is similar to that found in Bauer & Brandt (2004, who use a different method entirely).

The same CMCD model without any parameter adjustment gives an acceptable fit to this ACIS-S spectrum of X-1 ($\chi^2/dof = 77/97$); there is only a slight excess of the observed soft X-ray flux above the model. Simply letting one parameter free [e.g., $\tau = 0.96(0.69 - 1.3)$] improves the fit [$\chi^2/dof = 62/96$; F-test probability for no improvement is 5×10^{-6} ; Fig. 8b]. The inferred 0.3–8 keV luminosity is almost exactly the same as the mean value during the *XMM-Newton* observation. Therefore, there is no substantial difference in both the spectral shape and luminosity between the *XMM-Newton* and *Chandra* spectra of X-1. Fig. 8b shows little evidence for residual, emission line-like features that are apparently present in the X-1 spectrum extracted by Bauer & Brandt (2004), at somewhat unexpected energies (e.g., ~ 2.25 and 3.65 keV; their Fig. 4 and discussion). Therefore, these features of the spectra are likely data processing artifacts.

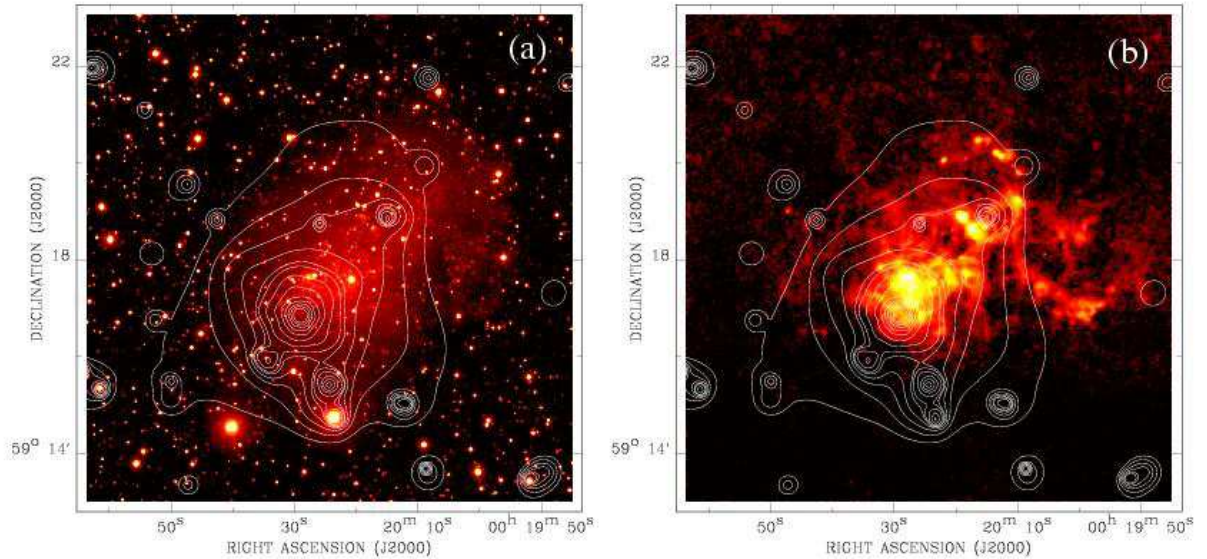


Fig. 9.— EPIC 0.5–2 keV intensity contours overlaid on (a) optical R-band and (b) $H\alpha$ images of IC 10 (Gil de Paz et al. 2003). The X-ray data have been adaptively smoothed with the CIAO routine *csmooth* with a signal-to-noise ratio of ~ 3 . The contours levels are at $1.1, 1.8, 2.9, 4.4, 6.2, 7.3, 11, 22, 44, 88, 183, 366,$ and $731 \times 10^{-3} \text{ cts s}^{-1} \text{ arcmin}^{-2}$.

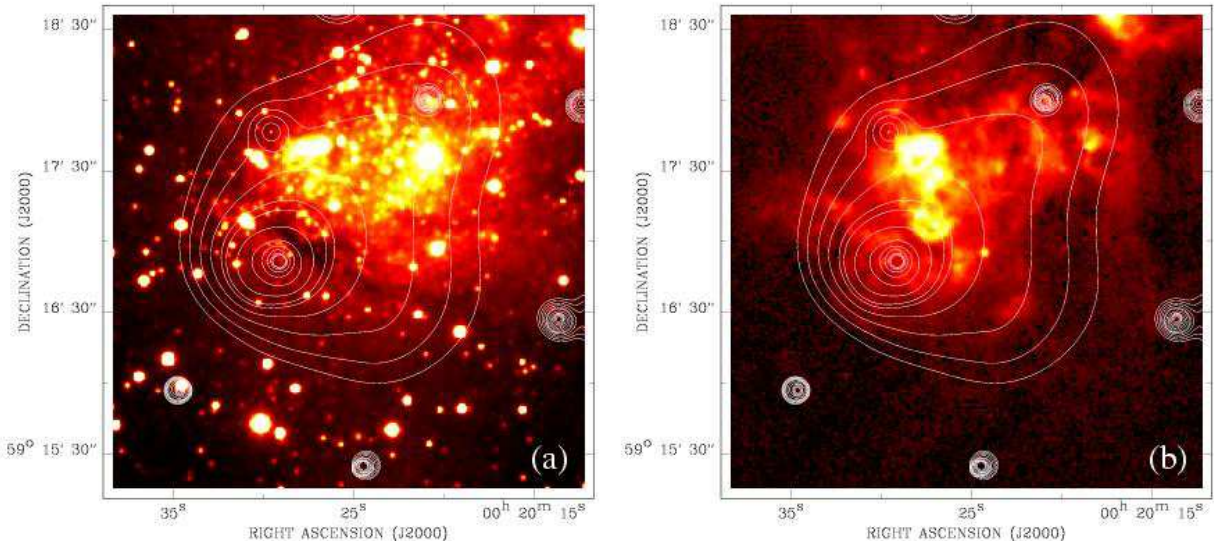


Fig. 10.— Close-up of the regions covered by the ACIS-S data. While the images are smoothed in the same way as in Fig. 9, the ACIS-S 0.7-4.5 keV intensity contours are at 3.9, 4.3, 4.9, 5.7, 6.7, 7.3, 9.3, 15, 27, 50, 100, 200, and 400×10^{-3} cts s^{-1} arcmin^{-2} .

3.3. Diffuse X-ray emission

There are clear indications for the presence of diffuse soft X-ray emission from IC 10. Fig. 9 shows the large-scale soft X-ray intensity distribution of the field. The distribution is calculated after a subtraction of the blank-sky background, which is normalized to the local source-removed intensity estimated in an annulus of off-axis radius $8' - 10'5$ in the IC 10 PN observation. In this step, we can approximately account for the background variation from one observation to another, particularly important for IC 10 because of its low Galactic latitude position. The soft X-ray structure near X-1 can only be examined in the high resolution *Chandra* observation (Fig. 10; see also Bauer & Brandt (2004)). To quantify the diffuse soft X-ray component, one needs to excise the detected sources and to estimate their residual contamination as well as sources below our detection limit. With the limited spatial resolution of the *XMM-Newton* data, a clean separation of the sources from the diffuse component is difficult. One might use a large EER to exclude a large fraction of source counts. However, the 90% EER at 1.5 keV, for example, is $\sim 50''$ on-axis and increases to $\sim 90''$ at an off-axis angle of $12'$. The adoption of such an EER for all the sources would leave regions too sparse for a diffuse emission study. A smaller EER is adequate for the bulk of faint sources ($\text{CR} \lesssim 0.01$ counts s^{-1}), which would leave acceptable amounts of contamination. For such a source, our adopted removal radius is twice the source detection radius for both the ACIS-S and PN data (or $\sim 75\%$ PSF EER for the PN data).

For brighter sources, we scale this radius by a factor of $1 + \log(CR/0.01)$. The adopted source removal regions are outlined in Figs. 3 and 5.

Of course, the remaining “diffuse” enhancement is still contaminated by the PSF wing of X-1 and other discrete sources. The on-axis PN PSF can be characterized by a King function,

$$I_{PSF}(R) = A \left[1 + \left(\frac{R}{r_0} \right)^2 \right]^{-\alpha}, \quad (1)$$

where R is the off-source angular distance and A is a normalization factor, while the core radius $r_0 \approx 5''.5$ or $5''.2$ and index $\alpha \approx 1.6$ or 1.5 for the the 0.5-2 keV or 2-4.5 keV bands, respectively². We compare the PSF with the radial profiles of the source-removed PN intensity around IC 10 X-1 by fitting the normalization and local uniform background (Fig. 11). The PSF gives a reasonably good fit to the profile in the 2-4.5 keV band ($\chi^2/dof = 269.8/237$). However, the fit in the 0.5-2 keV band is not acceptable ($\chi^2/dof = 522.9/237$); an excess of the observed intensity above the PSF is apparent at the annulus of the off-source distance between $\sim 0'.6 - 2'.4$. The total net CR in this annulus is ~ 0.022 (0.005) counts s^{-1} in the 0.5-2 keV (2-4.5 keV) band. We estimate that ~ 0.014 counts s^{-1} in the 0.5-2 keV band is due to the residual point-like contribution, assuming that it dominates the 2-4.5 keV band CR and has a mean spectrum similar to the best-fit absorbed power law of the *Chandra* detected sources (§3.1). The remaining ~ 0.008 counts s^{-1} in the 0.5-2 keV band may be a truly diffuse component. The luminosity of contribution is about the same as that of the detected sources within IC 10, excluding X-1 (§3.1). The faint point source contribution is probably a bit overestimated here, if it is less contaminated by the Galactic stellar population (which tends to contribute more soft X-rays) than the detected source spectrum.

We may also decompose the point-like and diffuse components in the PN data spectrally. We extract a spectrum of the diffuse component in the $0'.6 - 2'.4$ annulus. From the same region, we also obtain a background spectrum from the re-projected blank-sky data. The use of this background spectrum minimizes the effect of instrumental background variation across the detector. However, the sky background typically varies from one field to another. To account for this variation, we adjust the background spectrum by adding the spectral difference between the IC 10 and blank-sky data in an annulus between $5'.0 - 9'.3$ off X-1. In all of these spectral extractions, the source regions are removed from both the IC 10 and the blank-sky data. Fig. 12 shows the background-subtracted net spectrum of the diffuse X-ray component of IC 10. The apparent emission line features at ~ 1.01 and 1.35 , corresponding to the Ne X and Mg XI $K\alpha$ transitions, indicates that part of the component has a thermal

²http://xmm.vilspa.esa.es/external/xmm_user_support/documentation/uhb/node16.html

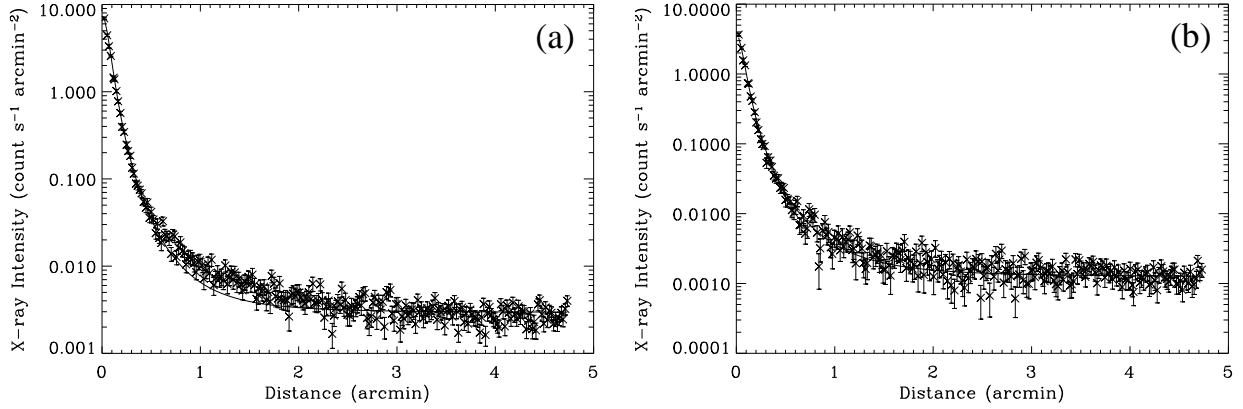


Fig. 11.— Radial surface intensity profiles around IC 10 X-1 in the PN 0.5-2 keV (a) and 2-4.5 keV bands (b). Background is not subtracted from the data, and is included in the PSF fits, which are shown as the solid lines.

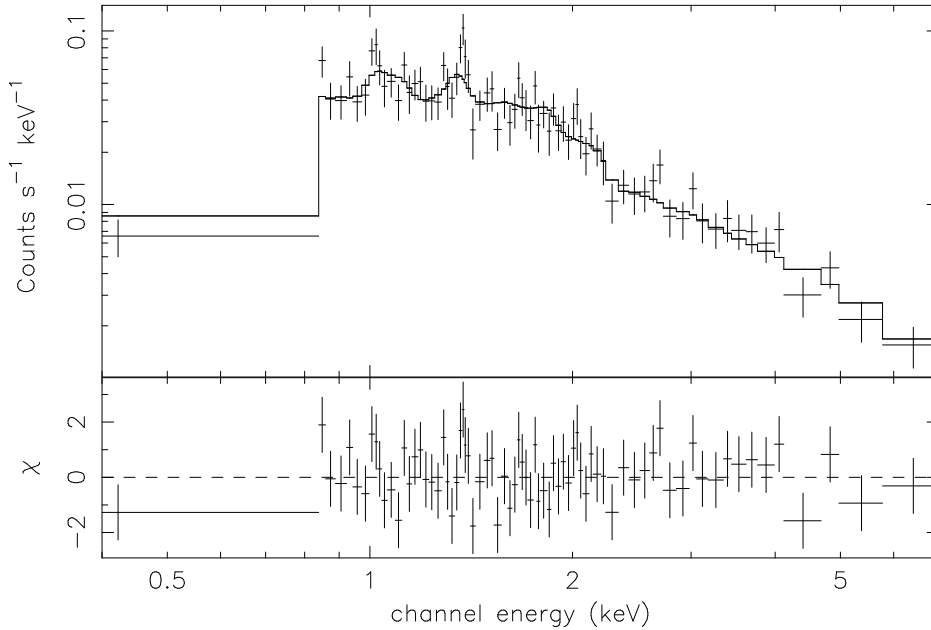


Fig. 12.— PN spectrum of the diffuse X-ray enhancement of IC 10, together with the fitted thermal plasma plus power law model.

origin. Therefore, we fit this spectrum with the combination of an optically thin thermal plasma (XSPEC *MEKAL* model) and a power law to characterize the residual point-like source contribution. The fit is satisfactory ($\chi^2/dof = 64.6/67$; Fig. 12) and gives reasonable model parameters: $kT = 0.30(0.20 - 0.50)$, metal abundance = $0.84(> 0.11)$, power law

photon index = 2.3(2.0 – 2.5), and $N_H = 1.1(0.61 – 1.43) \times 10^{22} \text{ cm}^{-2}$ (assuming the solar metal abundance for the absorbing gas). The index is marginally greater than that inferred from the fit to the accumulated *Chandra* source spectrum (§3.1), which is probably due, in part, to our demand for the same N_H for both the power law and the plasma components. Indeed, these two power laws (one from the source spectrum and the other from the spectral decomposition here) give comparable predictions of the relative contribution of point-like sources in the 0.5-2 keV and 2-4.5 keV bands. Thus we conclude that the residual point-like source contribution, corrected for the absorption, is $\sim 2 \times 10^{37} \text{ erg s}^{-1}$ in the 0.5-2 keV band and the corresponding hot gas luminosity is a factor of ~ 4 higher. If an extrapolation of the best-fit thermal plasma model to energies outside the band is a good approximation, the total cooling rate of the plasma should then be about $2 \times 10^{38} \text{ erg s}^{-1}$.

4. Discussion

4.1. Discrete X-ray sources

Following Wang (2004a), we estimate the contribution of background AGNs in the sources detected from the PN data. This estimate uses a X-ray source $\log N - \log S$ relation in the 0.5-2 keV band from the *Chandra* deep survey. We assume that these AGNs have a power law with a typical photon index of ~ 1.7 and are subject to an average foreground absorption of the Galactic H I column density $\sim 5 \times 10^{21} \text{ cm}^{-2}$. Accounting for both the sensitivity incompleteness and the Eddington bias of our source detection in the 0.5-7.5 keV band, we estimate the AGN contribution is ~ 20 . If the absorption is higher (e.g., including the column contribution from IC 10), the contribution would be smaller. Although this estimate is quite uncertain, both statistically and systematically (Wang 2004), it is clear that the bulk of our detected PN sources are either Galactic or associated with IC 10.

The identification of individual X-ray sources in the IC 10 field is generally not easy, because of the galaxy’s low Galactic latitude position ($b = -3.3$). In addition to the Galactic H I column density, there is evidence for substantial contributions from molecular gas in the Galaxy and/or gas inside IC 10. The comparison between the radio and H α fluxes of H II regions, for example, indicates $E_{B-V} \sim 2$ (Yang & Skillman 1993). From the Galactic relation $N_H/E_{B-V} = 4.8 \times 10^{21} \text{ cm}^{-2}$ (Bohlin, Savage, & Drake 1978), we infer $N_H \sim 1 \times 10^{22} \text{ cm}^{-2}$, which is quite similar to the X-ray-absorbing gas column density that we have estimated from the above spectral analysis of X-1 and the sources in the main body of IC 10.

Considering the general high extinction expected for the objects in the field, we first

use the Two Micron All Sky Survey (2MASS) All-Sky Catalog of Point Sources (Cutri et al. 2003) to search for potential counterparts. We cross-correlate the spatial positions of the objects in the catalog with those from Tables 1 and 2, using a matching radius of $4''$ for PN sources and $2''$ for ACIS sources. The radius is chosen to be greater than the 1σ statistical position uncertainty of almost all the sources. Table 3 presents the matching results, including the position offset of each match; there is no match with multiple 2MASS objects. The table also includes the J, H, and K_s magnitudes of the matched 2MASS objects; the 3σ limiting sensitivities of the catalog are 17.1, 16.4 and 15.3 mag in the three bands. The X-ray sources with the 2MASS matches tend to have soft X-ray spectral characteristics, having negative hardness ratios and/or being detected preferentially in the S band (Tables 1 and 2). These 2MASS objects, many of which also show up in optical images, should mostly be Galactic stars. The 2MASS matches with those few sources with relatively hard X-ray spectral characteristics (namely XP-16, XP-34, and XA-11) are all very faint (e.g. $K_s \gtrsim 14.6$); they may be stars in distant parts of the Galaxy. Some of the matches in Table 3 should represent chance projections of 2MASS objects within the matching regions. We estimate the expected number of such chance projections to be 0.25 for the ACIS sources and 2.6 for the PN sources, based on the surface number density of 2MASS objects within annuli of radius $4''$ - $15''$ around the X-ray sources.

We next use the NASA/IPAC Extragalactic Database and the SIMBAD Astronomical Database to search for identified objects within $2''$ of each X-ray source position. We find that XP-29/XA-9 matches with an unresolved nonthermal radio source (Yang & Skillman 1993; Chyzy et al. 2003), XP-9 with HD 1486 — an eclipsing binary of Algol type, and XP-25 with HL90 — an HII region in IC 10. Increasing the search radius to $4''$ only leads to one additional correspondence, i.e., XP-57 with the NRAO VLA sky survey radio source NVSS J002108+591132.

4.2. IC 10 X-1

We have shown that X-1 has a blackbody-like X-ray spectrum. The inferred inner disk temperature ($T_{in} \sim 1.1$ keV) is consistent with those found in LMC X-1, LMC X-3, and Cyg X-1 — stellar mass BH X-ray binaries. In contrast, X-ray binaries with intermediate mass BH candidates have substantially lower T_{in} values ($\sim 0.1 - 0.3$ keV; e.g., Wang et al. 2004). The spectrum of an accreting neutron star in an X-ray binary system is typically dominated by a power law component and/or an optically thin X-ray photo-ionized plasma (e.g., Paerels et al. 2000). Therefore, IC 10 X-1 is most likely a stellar mass BH associated with the W-R star [MAC92] 17A.

The only other known candidate for such an X-ray luminous BH/W-R binary system is Cyg X-3 at a distance of ~ 9 kpc in our Galaxy ($l, b = 79^\circ 8, 0^\circ 7$), although the true nature of this source remains uncertain (e.g., Mitra 1998). The X-ray spectrum of Cyg X-3 typically shows strong lines, which are interpreted as the evidence for a tenuous X-ray photo-ionized plasma, presumably in the stellar wind from the W-R companion star (Liedahl & Paerels 1996). But occasionally, the line emission weakens substantially, probably during a very high luminosity state (Smale et al. 1993). The spectrum in this state is very similar to that of IC 10 X-1 in terms of both T_{in} and the X-ray luminosity. Longer observations of IC 10 X-1 are needed to further the comparative study (e.g., to capture the low luminosity state of the source). Despite its projected location near the Galactic plane, IC 10 X-1 is still in a line of sight that is considerably less confusing and obscured than that of Cyg X-3. Therefore, the study of IC 10 X-1 may provide new insights into the end products of most massive stars (e.g., the progenitor mass required to form black holes in close binaries; e.g., Wellstein & Langer 1999; Clark & Crowther 2004).

4.3. Diffuse X-ray emission

Evidence for the diffuse soft X-ray emission in the immediate vicinity of IC 10 X-1 has also been presented by Bauer & Brandt (2004). From a comparison of the radial intensity profile around the source with the PSF of the *Chandra*, they find that a diffuse emission enhancement with a total ACIS-S CR of $\sim 1 \times 10^{-3}$ counts s^{-1} extends $\sim 17''$, a scale comparable to the radius of the nonthermal radio shell discovered by Yang & Skillman (1993). This result is not significantly affected by our removal of the CCD-readout streak, which contributes $\sim 16\%$ of the enhancement. But its morphology is changed from the slightly northeast-southwest extension before the removal (see Fig. 1 in Bauer & Brandt (2004)) to the northwest orientation after the removal (Fig. 4).

We have further shown that the lower surface brightness diffuse soft X-ray emission extends at least $\sim 2'$ (Fig. 9), and possibly as far as $\sim 4'$ (Fig. 10), northwest from X-1. The morphology of the emission seems to represent an extension of recent intense star-forming regions where the bulk of known W-R stars are located. The overall extent of the emission appears to outline the boundaries of prominent $H\alpha$ streamers/features; as illustrated by Wilcots & Miller (1998) with a high-quality $H\alpha$ image, these features correspond to the Shells 6 (located slightly southwest to X-1), 7 (northwest to X-1), 8 (around X-1), and possibly 4/5 further to the northwest. This morphological similarity suggests an association of the diffuse soft X-ray emission with the $H\alpha$ streamers, i.e., a scaled-up version of the 30 Doradus Nebula in the Large Magellanic cloud (Wang 1999).

The soft spectral characteristics of the diffuse X-ray emission indicates that it represents diffuse hot gas in IC 10. Our spectral analysis also shows marginal evidence for enhanced metal abundances. But with a temperature of a few 10^6 K, as we have inferred, this hot gas cannot be confined by the gravity of IC 10. Without sufficient cooling, the gas is likely to escape. Indeed, as in many other active star-forming galaxies (Wang et al. 2001), there is an apparent “missing” energy problem (Wang 2004b). With a typical mass-loss rate of $\sim 10^{-5} M_{\odot} \text{ yr}^{-1}$ and a wind speed of $\sim 10^3 \text{ km s}^{-1}$, a W-R star is expected to have a mechanical energy luminosity of $\sim 3 \times 10^{36} \text{ erg s}^{-1}$. The W-R star population (§1) alone could provide sufficient energy to balance the cooling of the diffuse soft X-ray-emitting gas ($2 \times 10^{38} \text{ erg s}^{-1}$; §3.3). Of course, stellar winds from other massive stars as well as supernova blastwaves together should supply substantially more energy. But this energy is not observed in X-ray radiation. Most likely, the energy is used to drive the expansion of the various observed energetic structures around recent massive star forming regions. This process is probably happening in the galaxy’s southeast portion, where the hot gas is apparently still confined, naturally explaining the overall morphological similarity between the diffuse soft X-ray emission and the $\text{H}\alpha$ streamer/features. Once the hot gas is out of the confinement of the ISM, the X-ray radiative cooling becomes even less efficient. This transition has probably occurred around previous star formation regions in the western portion of the galaxy. These regions, traced by large (probably quiescent) faint $\text{H}\alpha$ shells (Thurrow & Wilcots 2005; Wilcots & Miller 1998), show little diffuse X-ray enhancement.

5. Summary

We have conducted a careful analysis of the *XMM-Newton* and *Chandra* X-ray CCD observations of the nearby starburst galaxy IC 10. In particular, we have devised an effective method to remove the CCD-readout streaks of the bright source IC 10 X-1. The main results of our analysis are as follows:

- A list of 73 *XMM-Newton* and 28 *Chandra* detections of point-like sources in the IC 10 field is presented, including preliminary multi-wavelength identifications based on existing databases. While a large portion of these sources are likely to be foreground and background objects, those associated with IC 10 tend to show hard X-ray spectral characteristics consistent with high-mass X-ray binaries.
- We confirm that X-1 likely represents a BH/W-R binary system. The mean X-1 luminosity of $\sim 1.2 \times 10^{38} \text{ erg s}^{-1}$ in the 0.3-8.0 keV band is about the same during the *XMM-Newton* and *Chandra* observations. But the source shows large luminosity variation by a factor of up to ~ 6 on time scales of $\sim 10^4$ s. The spectrum of X-1

is well characterized by a Comptonized multi-color blackbody accretion disk with an inner disk temperature $T_{in} \approx 1.1$ keV, typical of those persistent X-ray binaries with stellar mass BHs (i.e., LMC X-1, LMC X-3, and Cyg X-1). For X-1, we infer the mass of the putative BH as $\sim 4 M_{\odot}$ if it is not spinning, or a factor of up to ~ 6 higher if the spinning is important.

- The presence of the diffuse soft X-ray emission in IC 10 is revealed. The emission is morphologically oriented along the optical main body and is greatly enhanced around most active star-forming regions of the galaxy. The extent of the emission resembles that of luminous H α streamers, emanating from starburst regions. The diffuse soft X-ray emission most likely arises from chemically-enriched hot gas with a characteristic temperature of ~ 0.3 keV and a total 0.5-2 keV luminosity of $\sim 8 \times 10^{37}$ erg s $^{-1}$. Although its total cooling rate ($\sim 2 \times 10^{38}$ erg s $^{-1}$) is still quite uncertain, this hot gas could be easily maintained by the mechanical energy input from the observed large W-R star population in the galaxy. But the X-ray radiation is unlikely to be the main cooling mechanism of the hot gas, which apparently powers various energetic ISM features observed around the starburst regions and will eventually escape from the galaxy.

These results demonstrate that IC 10 is a high-energy power house, hosting numerous energetic stellar and interstellar activities, which are most likely the end products of massive stars.

We thank the referee Franz Bauer for valuable comments on the work, which is supported by NASA through the grant NAG5-13582 and the Massachusetts Space Grant. This publication makes use of data products from the Two Micron All Sky Survey, which is a joint project of the University of Massachusetts and the Infrared Processing and Analysis Center/California Institute of Technology, funded by the National Aeronautics and Space Administration and the National Science Foundation.

REFERENCES

- Arnaud, K. A. 1996, in *Astronomical Data Analysis Software and Systems V*(ASP Conf. Series volume 101), eds. Jacoby G. and Barnes J., p17
- Balucinska-Church, M., & McCammon, D. 1992, *ApJ*, 400, 699
- Bauer, F., & Brandt, W. N. 2004, *ApJ*, 601, 67
- Bohlin, R. C., Savage, B. D., & Drake, J. F. 1978, *ApJ*, 224, 132
- Brandt, W. N., Ward, M. J., Fabian, A.C., & Hodge, P. W. 1997, *MNRAS*, 291, 709
- Chyzy, K. T., et al. 2003, *A&A*, 405, 513
- Clark, J. S., & Crowther, P. A. 2004, *A&A*, 414, 45
- Cutri, R. M., et al. 2003, *VizieR On-line Data Catalog*
- Crowther, P. A., Drissen, L., Abbott, J. B., Royer, P., & Smartt, S. J. 2003, *A&A*, 404, 483
- Davis, J. E. 2001, *ApJ*, 562, 575
- Demers, S., Battinelli, P., & Letarte, B. 2004, *A&A*, 424, 125
- Gil de Paz, A., Madore, B. F., & Pevunova, O. 2003, *ApJS*, 147, 29
- Jarrett, T. H., Chester, T., Cutri, R., Schneider, S. E., & Huchra, J. P. 2003, *AJ*, 125, 525
- Lequeux, J., et al. 1979, *A&A*, 80, 155
- Liedahl, D. A., & Paerels, F. 1996, *ApJL*, 468, 33
- Makishima, K., et al. 1986, *ApJ*, 308, 635
- Massey, P., Armanroff, T. E., & Conti, P. S. 1992, *AJ*, 103, 1159
- Massey, P., & Holmes, S. 2002, *ApJ*, 580, 35
- Mitra, A. 1998, *ApJ*, 499, 385
- Paerels, F., et al. 2000, *ApJL*, 533, 135
- Read, A. M., & Ponman, T. J. 2003, *A&A*, 409, 395
- Richer, M. G., et al. 2001, *A&A*, 370, 34

- Smale, A. P., et al. 1993, ApJ, 418, 894
- Stark, A. A., et al. 1992, ApJS, 79, 77
- Thurrow, J. C., & Wilcots, E. M. 2005, AJ, 129, 745
- Wang, Q. D. 1999, ApJL, 510, 139
- Wang, Q. D., et al. 2001, ApJL, 555, 99
- Wang, Q. D., Chaves, T., & Irwin, J. 2003, ApJ, 598, 969
- Wang, Q. D. 2004a, ApJ, 612, 156
- Wang, Q. D. 2004b, in Extraplanar Gas, ed. R. Braun (astro-ph/0410035)
- Wang, Q. D., et al. 2004, ApJ, 609, 113
- Wellstein, S., & Langer, N. 1999, A&A, 350, 148
- Wilcots, E. M., & Miller, B. W. 1998, AJ, 116, 2363
- Yang, H., & Skillman, E. D. 1993, AJ, 106, 1448
- Yao, Y., & Wang, Q. D. 2005, MNRAS, submitted

Table 1. *XMM-Newton* Source List

Source	XMMU Name	δ_x (")	CR (cts ks ⁻¹)	HR	HR1	Flag
(1)	(2)	(3)	(4)	(5)	(6)	(7)
1	J001834.79+591946.8	1.8	19.28 ± 2.23	–	–0.38 ± 0.10	B, S
2	J001845.81+592331.9	3.1	5.57 ± 1.44	–	–0.72 ± 0.18	S, B
3	J001855.81+591240.1	1.5	19.06 ± 1.93	–	–0.38 ± 0.09	S, B
4	J001857.44+590458.5	3.4	6.85 ± 1.67	–	–	B
5	J001902.38+591623.3	2.2	6.74 ± 1.12	–	0.70 ± 0.15	B, S
6	J001909.72+591916.0	2.7	4.74 ± 1.00	–	–	B, S
7	J001910.26+592455.9	3.7	3.76 ± 1.00	–	–	B, S
8	J001917.94+591231.9	2.2	6.89 ± 1.11	–	–0.28 ± 0.16	B, S
9	J001918.64+590820.7	0.3	529.36 ± 9.60	–0.72 ± 0.02	–0.11 ± 0.02	B, S, H
10	J001922.60+591541.7	3.3	2.85 ± 0.74	–	–	B
11	J001925.54+591417.5	2.1	5.34 ± 0.92	–	–0.39 ± 0.15	S, B
12	J001926.58+591103.5	3.2	3.12 ± 0.85	–	–	S, B
13	J001927.16+592423.6	3.1	4.30 ± 0.98	–	–	B, H
14	J001929.33+590420.9	3.0	7.93 ± 1.64	–	0.07 ± 0.19	B, S
15	J001938.11+591652.6	2.9	3.02 ± 0.64	–	–	B, S
16	J001944.06+591815.9	2.5	3.33 ± 0.66	0.47 ± 0.18	–	H, B
17	J001947.84+591711.5	2.0	3.74 ± 0.68	0.25 ± 0.19	–	B, H
18	J001949.48+590620.6	3.0	6.24 ± 1.26	–	–	B, S
19	J001949.69+591334.3	2.5	3.10 ± 0.66	–	–	B
20	J001950.60+590440.4	3.5	5.66 ± 1.32	–	–	B, S
21	J001951.82+591328.5	2.2	3.15 ± 0.64	–	–0.64 ± 0.16	S
22	J001952.36+590704.5	3.3	4.29 ± 1.00	–	–	B, S
23	J001952.73+590854.1	2.7	5.62 ± 1.01	0.49 ± 0.19	–	B, H
24	J002008.34+592144.5	2.0	4.72 ± 0.73	0.35 ± 0.17	–	B, H, S
25	J002008.36+591953.2	2.5	2.11 ± 0.51	–	–	B
26	J002008.84+591338.5	2.1	4.03 ± 0.67	–	0.58 ± 0.17	B, S
27	J002010.78+592547.2	2.0	6.61 ± 1.06	0.29 ± 0.18	–	B, H, S
28	J002012.48+591500.4	1.1	7.75 ± 0.82	0.06 ± 0.13	0.66 ± 0.12	B, S, H
29	J002015.10+591854.0	1.4	5.37 ± 0.72	–	0.16 ± 0.13	B, S
30	J002015.84+592637.2	2.8	4.05 ± 0.90	–	–	B, H
31	J002018.03+590732.0	1.7	10.96 ± 1.33	0.47 ± 0.12	0.71 ± 0.18	B, H, S
32	J002018.31+591834.5	2.8	1.92 ± 0.52	–	–	H
33	J002021.57+591900.1	2.0	3.52 ± 0.63	–	–	B, H, S
34	J002023.16+590812.8	2.0	6.80 ± 1.04	–	0.40 ± 0.18	B, S, H
35	J002023.46+591445.5	1.3	7.24 ± 0.83	–	–0.58 ± 0.10	S, B
36	J002024.47+591525.7	0.5	37.52 ± 1.70	–0.03 ± 0.06	0.61 ± 0.05	B, S, H

Table 1—Continued

Source	XMMU Name	δ_x (")	CR (cts ks ⁻¹)	HR	HR1	Flag
(1)	(2)	(3)	(4)	(5)	(6)	(7)
37	J002025.84+591844.6	1.6	4.15 ± 0.67	–	0.08 ± 0.20	B, S, H
38	J002027.03+590613.8	3.0	4.74 ± 1.05	–	–	B, S
39	J002029.10+591651.1	0.1	656.72 ± 6.82	–0.15 ± 0.01	0.61 ± 0.01	B, S, H
40	J002033.97+591112.0	3.2	1.79 ± 0.57	–	–	S
41	J002034.07+591031.9	2.0	4.13 ± 0.72	0.73 ± 0.14	–	B, H
42	J002034.12+591555.6	1.2	7.22 ± 0.87	–	–0.10 ± 0.13	B, S
43	J002036.20+592402.6	2.9	2.79 ± 0.67	–	–	B, S
44	J002042.27+591709.6	2.6	2.35 ± 0.56	–	–	B, H
45	J002042.63+591850.3	2.9	1.90 ± 0.49	–	–	B
46	J002047.38+591935.4	2.1	3.94 ± 0.64	0.35 ± 0.17	–	B, H, S
47	J002050.24+591528.3	2.9	2.09 ± 0.54	–	–	S, B
48	J002050.26+591505.1	2.7	2.41 ± 0.57	–	–	B
49	J002052.96+591647.4	2.4	2.54 ± 0.55	–	–	B, H
50	J002053.78+592106.4	3.3	1.52 ± 0.51	–	–	S
51	J002058.62+590833.8	3.0	3.67 ± 0.85	–	–	B
52	J002100.75+591104.9	3.0	3.28 ± 0.73	–	–	S, B
53	J002101.69+591519.5	2.1	3.66 ± 0.68	–	0.26 ± 0.16	S, B
54	J002102.62+592158.0	1.8	6.32 ± 0.90	–0.00 ± 0.19	0.46 ± 0.17	B, S, H
55	J002103.82+590957.4	2.2	5.62 ± 0.94	0.87 ± 0.10	–	H, B
56	J002104.70+591540.2	1.8	4.61 ± 0.73	–	–0.47 ± 0.13	S, B
57	J002108.72+591134.4	2.6	3.78 ± 0.76	–	–	B, S, H
58	J002114.93+590844.5	1.7	11.65 ± 1.43	–	–0.33 ± 0.12	B, S
59	J002117.67+591839.9	3.4	2.26 ± 0.63	–	–	B
60	J002121.44+590905.7	0.9	40.00 ± 2.45	–	–0.26 ± 0.06	B, S
61	J002125.43+591904.2	1.8	6.02 ± 0.89	–	–0.59 ± 0.13	B, S
62	J002131.27+591428.0	2.6	4.04 ± 0.83	–	–	B, S
63	J002132.53+591313.6	3.1	3.88 ± 0.86	–	–	B
64	J002134.56+591443.6	2.8	3.17 ± 0.75	–	–	B, S
65	J002139.04+592243.4	1.9	9.09 ± 1.30	–	–0.32 ± 0.13	S, B
66	J002142.96+591207.3	3.4	3.61 ± 0.95	–	–	B
67	J002144.80+591730.8	3.4	3.08 ± 0.84	–	–	B
68	J002144.98+590736.2	3.3	5.82 ± 1.41	–	–	B
69	J002151.67+590820.1	3.5	5.68 ± 1.40	–	–	B, H
70	J002155.38+591008.5	2.6	7.60 ± 1.46	–	–	B, S
71	J002158.87+591326.7	1.3	25.98 ± 2.19	–	–0.28 ± 0.08	B, S
72	J002203.62+591515.4	3.9	4.01 ± 1.11	–	–	B

Table 1—Continued

Source	XMMU Name	δ_x (")	CR (cts ks ⁻¹)	HR	HR1	Flag
(1)	(2)	(3)	(4)	(5)	(6)	(7)
73	J002209.37+591357.6	1.7	19.79 ± 2.05	–	–0.09 ± 0.10	B, S

Note. — The definition of the bands: 0.5–1 (S1), 1–2 (S2), 2–4.5 (H1), and 4.5–7.5 keV (H2). In addition, S=S1+S2, H=H1+H2, and B=S+H. Column (1): Generic source number. (2): *XMM-Newton* X-ray Observatory (unregistered) source name, following the *XMM-Newton* naming convention and the IAU Recommendation for Nomenclature (<http://cdsweb.u-strasbg.fr/iau-spec.html>). (3): Position uncertainty (1σ) calculated from the maximum likelihood centroiding. (4): On-axis source broad-band count rate — the sum of the exposure-corrected count rates in the four bands. (5-6): The hardness ratios defined as $HR = (H - S2)/(H + S2)$, and $HR1 = (S2 - S1)/S$, listed only for values with uncertainties less than 0.2. (7): The label “B”, “S”, or “H” mark the band in which a source is detected with the most accurate position that is adopted in Column (3).

Table 2. *Chandra* Source List

Source	CXOU Name	δ_x (")	CR (cts ks ⁻¹)	HR	HR1	Flag
(1)	(2)	(3)	(4)	(5)	(6)	(7)
1	J001954.74+591721.5	1.7	0.40 ± 0.21	–	–	S, B
2	J002004.91+591507.4	0.7	0.62 ± 0.25	–	–	B, H
3	J002008.41+591540.0	0.4	0.64 ± 0.22	–	–	B, H
4	J002009.23+591818.3	0.9	0.44 ± 0.20	–	–	B, H
5	J002011.49+591627.0	0.6	0.32 ± 0.17	–	–	B, H
6	J002012.54+591757.8	0.3	0.72 ± 0.23	–	–	H, B
7	J002012.75+591500.8	0.1	5.42 ± 0.56	0.27 ± 0.12	0.90 ± 0.10	B, S, H
8	J002013.75+591626.6	0.2	2.34 ± 0.40	–	1.00 ± 0.11	B, S, H
9	J002015.04+591853.5	0.2	2.00 ± 0.36	–	0.88 ± 0.11	B, S
10	J002016.75+591556.2	0.8	0.20 ± 0.16	–	–	H
11	J002020.99+591758.6	0.1	12.40 ± 0.82	0.79 ± 0.05	1.00 ± 0.16	H, B, S
12	J002021.59+591901.5	0.5	1.60 ± 0.51	–	–	B, H
13	J002022.92+591538.4	0.7	0.27 ± 0.17	–	–	B
14	J002023.59+591444.0	0.1	4.02 ± 0.55	–	0.44 ± 0.14	B, S
15	J002024.54+591524.9	0.1	7.41 ± 0.66	0.13 ± 0.10	1.00 ± 0.07	B, H, S
16	J002026.11+591844.7	0.5	0.60 ± 0.31	–	–	S, B
17	J002026.68+591454.7	0.3	0.54 ± 0.22	–	–	S, B
18	J002029.17+591651.2	0.0	170.86 ± 3.14	0.20 ± 0.02	0.94 ± 0.01	B, H, S
19	J002030.74+591743.8	0.7	0.31 ± 0.17	–	–	B, H
20	J002034.67+591556.8	0.2	2.45 ± 0.40	–	0.79 ± 0.14	B, S, H
21	J002038.76+591740.7	0.3	0.90 ± 0.25	–	–	B, H
22	J002040.14+591435.3	0.8	0.67 ± 0.46	–	–	S
23	J002041.41+591712.4	0.9	0.43 ± 0.38	–	–	H
24	J002046.45+591731.4	0.4	0.61 ± 0.48	–	–	S, B
25	J002047.30+591320.2	0.7	0.94 ± 0.51	–	–	B, S
26	J002050.06+591504.9	2.3	0.37 ± 0.46	–	–	B
27	J002050.18+591408.7	0.8	0.41 ± 0.49	–	–	B, H
28	J002052.81+591648.5	0.4	1.11 ± 0.52	–	–	B, H, S

Note. — The definition of the bands: 0.3–0.7 (S1), 0.7–1.5 (S2), 1.5–3 (H1), and 3–7 keV (H2). In addition, S=S1+S2, H=H1+H2, and B=S+H. Column (1): Generic source number. (2): *Chandra* X-ray Observatory (unregistered) source name, following the *Chandra* naming convention and the IAU Recommendation for Nomenclature (e.g., <http://cdsweb.u-strasbg.fr/iau-spec.html>). (3): Position uncertainty (1σ) calculated from the maximum likelihood centroiding. (4): On-axis source broadband count rate — the sum of the exposure-corrected count rates in the four bands. (5-6): The

hardness ratios defined as $HR = (H - S2)/(H + S2)$, and $HR1 = (S2 - S1)/S$, listed only for values with uncertainties less than 0.2. (7): The label “B”, “S”, or “H” mark the band in which a source is detected with the most accurate position that is adopted in Column (3).

Table 3. Source Identification

Source	2MASS ID Name	$\delta_{x,o}$ (")	J, H, K _s (mag)
XP-1	J001834.91+591947.6	1.2	12.4 11.7 11.5
XP-3	J001855.89+591240.6	0.8	12.8 12.1 11.9
XP-9	J001918.74+590820.3	0.9	6.9 6.8 6.8
XP-11	J001925.62+591419.1	1.7	14.0 13.3 13.1
XP-12	J001926.70+591105.4	2.1	14.2 13.7 13.6
XP-16	J001944.20+591812.5	3.6	15.3 14.9 14.7
XP-19	J001949.37+591333.7	2.6	15.5 14.7 14.6
XP-21	J001951.75+591327.1	1.5	11.6 11.2 11.1
XP-34	J002023.22+590814.0	1.2	16.2 15.7 14.5
XP-35/XA-14	J002023.51+591444.7	1.0	8.8 8.5 8.5
XP-37/XA-16	J002025.98+591845.3	1.3	15.4 14.4 14.7
XP- 38	J002026.57+590615.6	4.0	15.1 14.6 14.3
XP-40	J002034.39+591114.1	3.8	15.1 14.6 14.3
XP-41	J002033.80+591033.5	2.6	13.0 12.2 12.0
XP-42/XA-20	J002034.58+591557.3	3.9	13.9 13.3 13.1
XP-43	J002036.24+592405.6	3.0	16.4 15.8 15.4
XP-45	J002042.67+591851.4	1.1	15.1 14.5 14.4
XP-47	J002050.13+591525.9	2.6	15.3 14.6 14.3
XP-50	J002053.89+592108.2	2.0	12.2 11.6 11.4
XP-52	J002101.03+591104.5	2.2	14.9 14.1 14.0
XP-53	J002101.55+591518.1	1.8	10.6 9.9 9.7
XP-56	J002104.59+591539.9	0.9	11.2 10.9 10.7
XP-58	J002114.77+590845.5	1.6	10.9 10.6 10.5
XP-60	J002121.38+590905.3	0.6	11.0 10.6 10.5
XP-61	J002125.69+591904.9	2.1	14.0 13.5 13.2
XP-65	J002139.00+592243.3	0.3	14.4 13.8 13.5
XP-71	J002158.82+591327.2	0.7	11.8 11.4 11.2
XP-73	J002209.58+591401.1	3.8	12.4 12.0 11.9
XA-11	J002020.90+591759.0	0.8	16.4 15.4 15.5
XA-13	J002022.80+591539.0	1.1	13.5 13.2 13.1
XA-17	J002026.61+591455.9	1.3	13.7 13.0 12.7
XA-22	J002040.10+591435.5	0.3	10.8 10.4 10.2
XA-24	J002046.44+591731.8	0.4	15.4 14.8 14.4
XA-25	J002047.26+591321.2	1.1	14.8 14.1 13.9

